scientific reports

Check for updates

OPEN

Evaluation of different ^{89}Zr-labeled synthons for direct labeling and tracking of white blood cells and stem cells in healthy athymic mice

Aditya Bansal[1], Shalini Sharma[1], Benedikt Klasen[2], Frank Rösch[2] & Mukesh K. Pandey[1]✉

Cell based therapies are evolving as an effective new approach to treat various diseases. To understand the safety, efficacy, and mechanism of action of cell-based therapies, it is imperative to follow their biodistribution noninvasively. Positron-emission-tomography (PET)-based non-invasive imaging of cell trafficking offers such a potential. Herein, we evaluated and compared three different ready-to-use direct cell radiolabeling synthons, [^{89}Zr]Zr-DFO-Bn-NCS, [^{89}Zr]Zr-Hy$_3$ADA^5-NCS, and [^{89}Zr]Zr-Hy$_3$ADA^5-SA for PET imaging-based trafficking of white blood cells (WBCs) and stem cells (SCs) up to 7 days in athymic nude mice. We compared the degree of ^{89}Zr complexation and percentage of cell radiolabeling efficiencies with each. All three synthons, [^{89}Zr]Zr-DFO-Bn-NCS, [^{89}Zr]Zr-Hy$_3$ADA^5-NCS, and [^{89}Zr]Zr-Hy$_3$ADA^5-SA, were successfully prepared, and used for radiolabeling of WBCs and SCs. The highest cell radiolabeling yield was found for [^{89}Zr]Zr-DFO-Bn-NCS, followed by [^{89}Zr]Zr-Hy$_3$ADA^5-NCS, and [^{89}Zr]Zr-Hy$_3$ADA^5-SA. In terms of biodistribution, WBCs radiolabeled with [^{89}Zr]Zr-DFO-Bn-NCS or [^{89}Zr]Zr-Hy$_3$ADA^5-NCS, were primarily accumulated in liver and spleen, whereas SCs radiolabeled with [^{89}Zr]Zr-DFO-Bn-NCS or [^{89}Zr]Zr-Hy$_3$ADA^5-NCS were found in lung, liver and spleen. A high bone uptake was observed for both WBCs and SCs radiolabeled with [^{89}Zr]Zr-Hy$_3$ADA^5-SA, suggesting in-vivo instability of [^{89}Zr]Zr-Hy$_3$ADA^5-SA synthon. This study offers an appropriate selection of ready-to-use radiolabeling synthons for noninvasive trafficking of WBCs, SCs and other cell-based therapies.

Safety and efficacy are the two main pillars of any therapeutics and cell-based therapies and imaging are no exception. Not much is known, to effectively assess the biodistribution, clearance and efficacy of cell-based therapies due to the absence of an appropriate noninvasive imaging tool. In vivo cell tracking could provide information about distribution, localization, and clearance of various cell-based therapies including immune cells (CAR-T cells), stem cells and hepatocytes post-administration in the body. There are various non-invasive molecular imaging modalities that could be employed to track cell based therapies including optical imaging via fluorescence imaging (FLI)[1,2], bioluminescence imaging (BLI)[3,4], and ultrasound-guided photoacoustic imaging (PA)[5–7]. Radiology imaging including magnetic resonance imaging (MRI)[8–10], computed tomography (CT)[11–13], and nuclear medicine imaging such as positron emission tomography (PET)[14–18] and single photon emission computed tomography (SPECT)[19,20], could also be employed to effectively measure the distribution, localization, and clearance of various cell-based therapies over time and to shed light on safety and efficacy.

Among various imaging modalities, optical imaging modalities are restricted to small animals due to limited tissue penetration (1–2 mm) in humans. MRI and CT provide high resolution anatomical information, but have low sensitivity in both animals and humans. Both PET and SPECT are advantageous over other techniques and are often integrated with CT and MRI. The PET/CT or SPECT/CT or PET/MRI provide quantitative and temporal distribution of immune and stem cells in animals and patients with no limitation of tissue penetration due to high energy gammas[21–24].

Cells can be radiolabeled either directly or indirectly[25]. Direct cell radiolabeling consists of ex-vivo radiolabeling of cells prior to their administration into body followed by short-term (< 7 days) in vivo tracking of these

[1]Division of Nuclear Medicine, Department of Radiology, Mayo Clinic, Rochester, MN 55906, USA. [2]Department of Chemistry-TRIGA Site, Johannes Gutenberg University, Mainz, Germany. ✉email: pandey.mukesh@mayo.edu

radiolabeled cells. The potential limitation of the direct cell labeling approach is the short-term tracking capability due to decay of the radioactivity over time and or efflux of radiotracer or instability of the labeled radioactive tag over time. On the other hand, the indirect cell radiolabeling method is based on transfection of a reporter gene (e.g., sodium iodide symporter (NIS)[26], simplex herpes virus type -1 thymidine kinase (HSV1-tk) etc.) in the cells that selectively takes up the respective radioactive reporter probe in the cells upon exposure to its respective reporter probe. If the administered cells keep expressing reporter protein after administration, then repeated systemic administration of its reporter probe allows long term-visualization of administered cells. Although the indirect cell labeling approach allows long term visualization of administered cells, genetic modification for cell labeling remains a regulatory hurdle.

Cell radiolabeling using a direct radiolabeling approach with various SPECT radiopharmaceuticals such as [^{99m}Tc]Tc-HMPAO ($t_{1/2}$ = 6.01 h)[27–29], and [^{111}In]In-oxine ($t_{1/2}$ = 68.2 h)[30–33] have been used to track leukocytes for infection and inflammation imaging over the past four decades. SPECT is a powerful clinical imaging tool with lower usage cost than PET since an onsite cyclotron is not needed. PET, however, has many advantages over SPECT including two to threefold higher sensitivity, superior spatial resolution in the clinical setting, and with its quantitative nature it is a preferred imaging modality for tracking a single cell or small number of administered radiolabeled cells with more precise quantification and hence, requires lower radiation exposure[34]. Examples of commercial PET probes used to label cells include [^{18}F]FDG ($t_{1/2}$ = 109.7 min, β^+ = 97%)[35], [^{64}Cu]Cu-PTSM ($t_{1/2}$ = 12.7 h, β^+ = 17.9%)[36] and [^{68} Ga]Ga-oxine ($t_{1/2}$ = 68 min, β^+ = 88.8%)[37,38].

Recently, among various PET radioisotopes, zirconium-89 (β^+ = 22.3%) is gaining popularity for cell tracking due to its well established cyclotron-mediated production, longer half-life of 3.27 days and low average positron energy ($E_{\beta+}$ = 0.395 MeV). This enables monitoring of radiolabeled cells up to 3-weeks, either through direct cell labeling (also called non-specific cell labeling agents)[39,40] or indirect labeling mediated through antibodies[41,42], peptides[43], proteins[44] and nanoparticles[45–47].

Various chelators used for the radiolabeling of cells with ^{89}Zr are tropolone, malonate, hydroxamates, and oxine (8-hydroxyquinoline). Among these, oxine forms a lipophilic complex with ^{89}Zr and enters the cells passively. To date, [^{89}Zr]Zr-oxine is a commonly used radiotracer to label various cells including tumor cell lines[48,49], bone marrow cells[50,51], T cells[52], NK cells[53], white blood cells (WBCs)[54], stem cells (SCs)[55] and leukocytes[56]. However, efflux of ^{89}Zr from cells labeled with [^{89}Zr]Zr-oxine remains a challenge. Recently, Friberger et al. reported a one-step clinically translatable method of synthesis of [^{89}Zr]Zr-oxine with a cell labeling efficiency of 61–68% with human decidual stromal cells (hDSCs), bone marrow-derived macrophages (rMac) and human peripheral blood mononuclear cells (hPBMCs). However, a 29–38% apparent efflux of ^{89}Zr from the labeled cells raised a further concern of radiotoxicity and non-specificity of the signal[57].

Besides [^{89}Zr]Zr-oxine, the other reported method of cell labeling was covalent attachment of radiolabeled [^{89}Zr]Zr-DFO-Bn-NCS complex with the primary amines present on the cell surface proteins to form stable thiourea bonds, which has solved the efflux problem observed with [^{89}Zr]Zr-oxine[57–60]. The [^{89}Zr]Zr-DFO-Bn-NCS has been successfully used to radiolabel mouse melanoma cells, mouse dendritic cells and human mesenchymal stem cells with insignificant efflux of free ^{89}Zr from [^{89}Zr]Zr-DFO-Bn-NCS over time (7 days-post radiolabeling)[58]. Additionally, a better version of the DFO chelator as DFO* has been developed to further strengthen the stability of ^{89}Zr complexation and has shown lower bone uptake over time[61]. Various other chelators are also being developed to address in vivo stability of the ^{89}Zr complex over time[62–66].

In this work, we have optimized and compared the radiolabeling yields of WBCs and SCs using three different ready-to-use labeling synthons [^{89}Zr]Zr-Hy$_3$ADA^5-NCS[66], [^{89}Zr]Zr-Hy$_3$ADA^5-SA[66] and [^{89}Zr]Zr-DFO-Bn-NCS[57–60] (Fig. 1), and evaluated their applications in cell trafficking to better understand the biodistribution/pharmacokinetics of cell based therapies**.** This approach could be extended to various other cell-based therapies like CAR-T cell therapy.

Results and discussion

Production of [^{89}Zr]ZrCl$_4$ and radiosynthesis of [^{89}Zr]Zr-DFO-Bn-NCS, [^{89}Zr]Zr-Hy$_3$ADA^5-NCS and [^{89}Zr]Zr-Hy$_3$ADA^5-SA. The PET isotope ^{89}Zr was produced and purified in-house using a cyclotron as described earlier by Pandey et al.[67–70] in a high apparent molar activity of 17.0–23.13 GBq/µmol, as assessed by complexing purified [^{89}Zr]ZrCl$_4$ with different amounts of DFO-Bn-NCS (Fig. S1, supplementary figure). All three synthons were successfully conjugated with ^{89}Zr at 37 °C; pH 7.5–8.0 for 30 min in 72–98% radiolabeling yield. The DFO-Bn-NCS showed the highest complexation yield of 97.76 ± 0.31% (n = 3) followed by Hy$_3$ADA^5-NCS, 88.85 ± 0.05% (n = 3) and Hy$_3$ADA^5-SA, 71.58 ± 0.47% (n = 3) (Table 1, Fig. 2). These results indicate that acyclic chelator DFO-Bn-NCS imparts faster binding kinetics as compared to hybrid "cyclic-acyclic' chelators Hy$_3$ADA^5-NCS and Hy$_3$ADA^5-SA. This is consistent with the complexation yield reported in our previous work, where a higher complexation yield was observed for DFO derivatives as compared to Hy$_3$ADA derivatives[66].

Radiolabeling of WBCs and SCs. All three synthons were successfully employed to radiolabel WBCs and SCs, however their cell radiolabeling yield varied in the following order [^{89}Zr]Zr-DFO-Bn-NCS > [^{89}Zr]Zr-Hy$_3$ADA^5-NCS > [^{89}Zr]Zr-Hy$_3$ADA^5-SA. For WBCs, the radiolabeling efficiency with [^{89}Zr]Zr-DFO-Bn-NCS was 22.77 ± 5.02% (n = 3) as compared to 3.18 ± 0.86%; (n = 3) with [^{89}Zr]Zr-Hy$_3$ADA^5-NCS and only 1.5 ± 0.28%; (n = 2) with [^{89}Zr]Zr-Hy$_3$ADA^5-SA (Fig. 3). The radiolabeling efficiency for SCs with [^{89}Zr]Zr-DFO-Bn-NCS was 41.83 ± 5.02% (n = 3) as compared to 6.57 ± 0.47% (n = 2) with [^{89}Zr]Zr-Hy$_3$ADA^5-NCS and only 3.59 ± 0.27% (n = 2) with [^{89}Zr]Zr-Hy$_3$ADA^5-SA (Fig. 4). The radiolabeled WBCs and SCs showed ~ 90–95% viability as per trypan blue exclusion cell viability assay. The difference in radiolabeling efficiencies between WBCs and SCs were expected due to the difference in their cell sizes and availability of surface proteins for

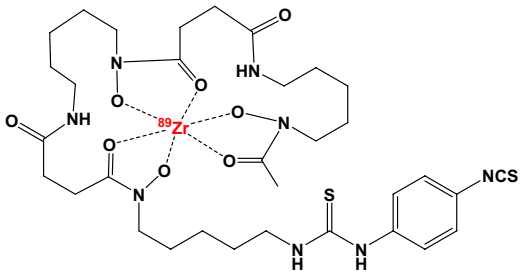

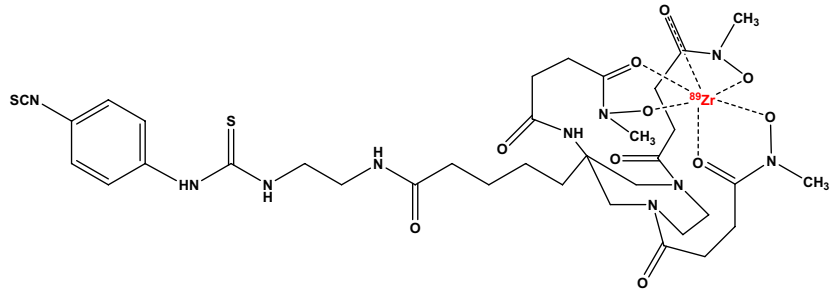

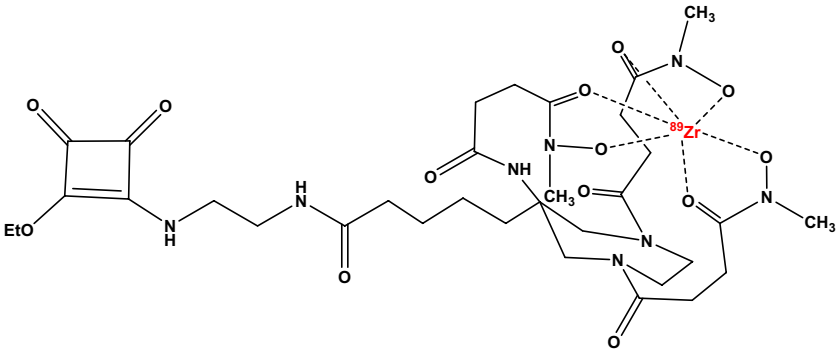

Figure 1. Chemical structures of [^{89}Zr]Zr-DFO-Bn-NCS, [^{89}Zr]Zr-Hy$_3$ADA^5-NCS and [^{89}Zr]Zr- Hy$_3$ADA^5-SA.

Labeling condition	Reaction time	Percentage of ^{89}Zr complexation with different synthons (average ± SD)		
		[^{89}Zr]Zr-DFO-Bn-NCS (n = 3)	[^{89}Zr]Zr-Hy$_3$ADA^5-NCS (n = 3)	[^{89}Zr]Zr-Hy$_3$ADA^5-SA (n = 3)
37 °C, pH 7.5–8.0	10 min	91.83 ± 2.07	74.83 ± 5.38	59.08 ± 5.28
	20 min	95.89 ± 0.51	82.27 ± 1.53	68.27 ± 3.26
	30 min	97.76 ± 0.31	88.85 ± 0.05	71.58 ± 0.47

Table 1. Percentage of ^{89}Zr complexation with DFO-Bn-NCS, Hy$_3$ADA^5-NCS and Hy$_3$ADA^5-SA at different reaction times.

conjugation and radiolabeling. The average cell size in the cell population was measured by TC10 cell counter (Biorad Laboratories, Inc. Hercules, CA) and found to be 4–10 µm for WBCs and 12–20 µm for SCs. Within a cell type, more cell labeling was observed with [^{89}Zr]Zr-DFO-Bn-NCS as compared to [^{89}Zr]Zr-Hy$_3$ADA^5-NCS and [^{89}Zr]Zr-Hy$_3$ADA^5-SA. Further variation in radiolabeling yield could be explained by two aspects that may affect the cell radiolabeling yield. First, the degree of ^{89}Zr-complexation with each chelator, where [^{89}Zr]Zr-DFO-Bn-NCS had shown a relatively higher degree of ^{89}Zr-complexation to begin with as compared to [^{89}Zr]Zr-Hy$_3$ADA^5-NCS (~ 9% lower than [^{89}Zr]Zr-DFO-Bn-NCS) and [^{89}Zr]Zr-Hy$_3$ADA^5-SA (~ 27% lower than [^{89}Zr]Zr-DFO-Bn-NCS). Second, the steric hindrance caused by hybrid chelators like Hy$_3$ADA^5-NCS and Hy$_3$ADA^5-SA during conjugation with cell surface proteins, suggesting a need to extend the length of the linkers in the case of Hy$_3$ADA^5-NCS and Hy$_3$ADA^5-SA chelators. The radiolabeling of cells with [^{89}Zr]ZrCl$_4$ as a negative control showed extremely poor radiolabeling efficiency for WBCs (0.80 ± 0.04%; n = 3) and stem cells

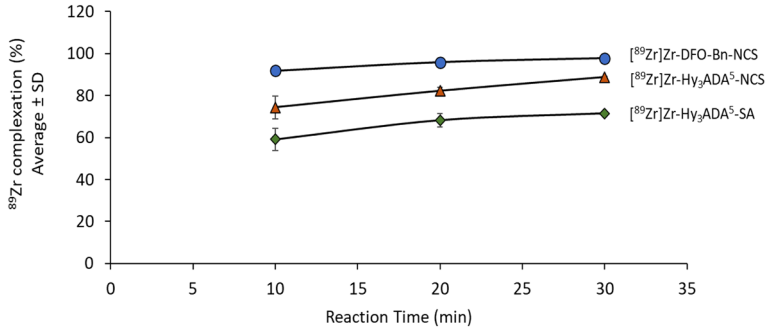

Figure 2. Percentage of ^{89}Zr complexation with DFO-Bn-NCS, Hy_3ADA^5-NCS and Hy_3ADA^5-SA at different reaction times.

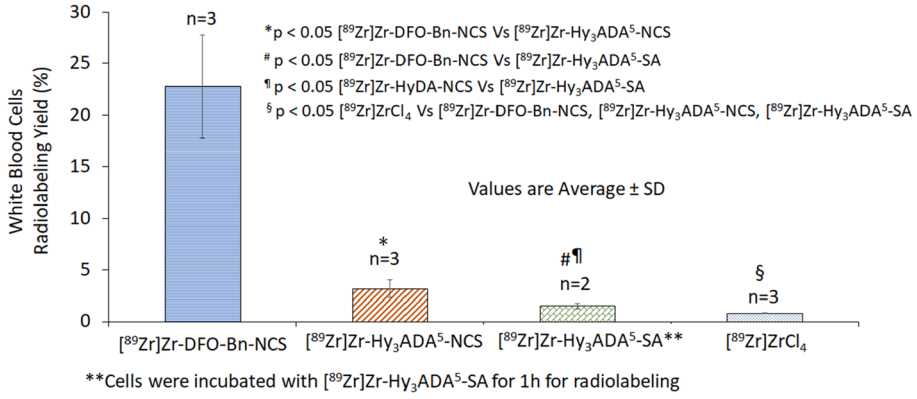

Figure 3. Radiolabeling of white blood cells (WBCs) with [^{89}Zr]Zr-DFO-Bn-NCS, [^{89}Zr]Zr-Hy_3ADA^5-NCS, [^{89}Zr]Zr-Hy_3ADA^5-SA and [^{89}Zr]$ZrCl_4$.

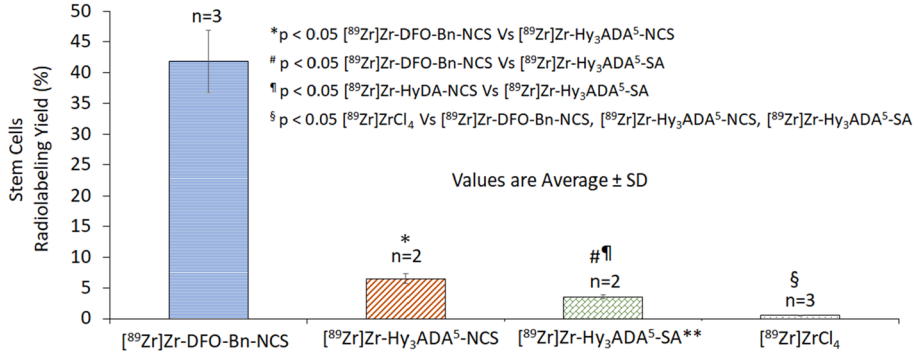

Figure 4. Radiolabeling of stem cells with [^{89}Zr]Zr-DFO-Bn-NCS, [^{89}Zr]Zr-Hy_3ADA^5-NCS, [^{89}Zr]Zr-Hy_3ADA^5-SA and [^{89}Zr]$ZrCl_4$.

(0.60 ± 0.01%; n = 3) as compared to radiolabeling efficiencies observed with the [^{89}Zr]Zr-DFO-Bn-NCS, [^{89}Zr]Zr-Hy_3ADA^5-NCS and [^{89}Zr]Zr-Hy_3ADA^5-SA.

Small animal PET imaging and biodistribution of ^{89}Zr labeled WBCs. Small animal PET imaging and biodistribution of WBCs were performed independently after radiolabeling of WBCs with three different radiolabeling synthons, [^{89}Zr]Zr-DFO-Bn-NCS, [^{89}Zr]Zr-Hy_3ADA^5-NCS, and [^{89}Zr]Zr-Hy_3ADA^5-SA to assess any variation in pharmacokinetics of WBCs radiolabeled with different synthons in healthy athymic mice (Fig. 5). After intravenous injection of WBCs-labeled with [^{89}Zr]Zr-DFO-Bn-NCS, the majority of the radioactivity was observed in the liver and spleen, and remained significantly high at all time points (4 h, 2 days, 4 days, 7 days). Importantly, no bone uptake was observed at any time point over 7 days indicating good in vivo stability

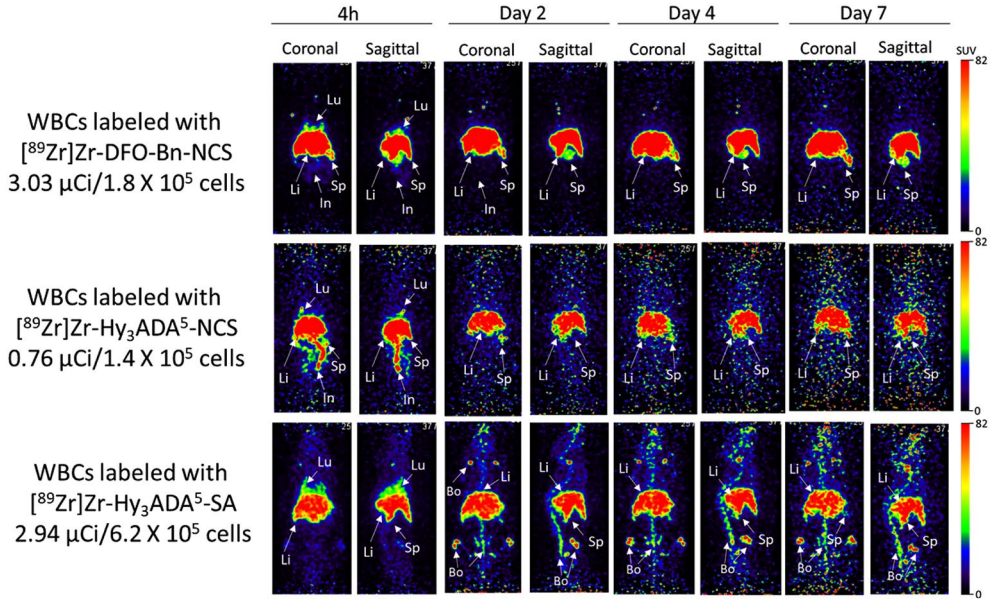

Figure 5. Representative coronal and sagittal PET maximum intensity projection (MIP) images showing distribution of WBCs labeled with [^{89}Zr]Zr-DFO-NCS, [^{89}Zr]Zr-Hy$_3$ADA^5-NCS and [^{89}Zr]Zr-Hy$_3$ADA^5-SA synthons in athymic nude mice at different time points post-injection.

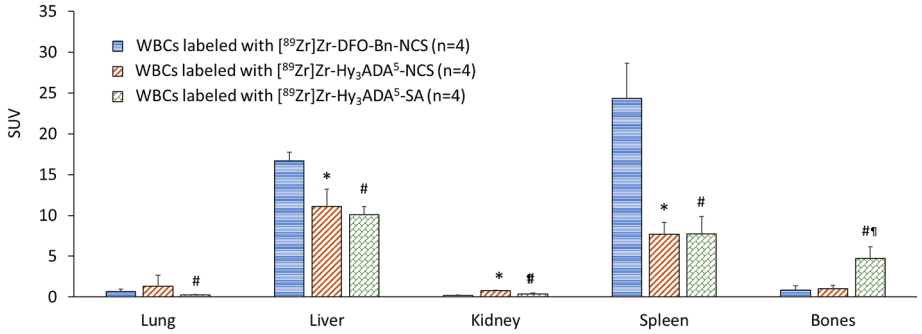

Figure 6. Uptake (SUV) and biodistribution of WBCs labeled with [^{89}Zr]Zr-DFO-NCS, [^{89}Zr]Zr-Hy$_3$ADA^5-NCS and [^{89}Zr]Zr-Hy$_3$ADA^5-SA synthons in major organs of athymic nude mice at day 7 post-injection. $^{*}p < 0.05$ WBCs labeled with [^{89}Zr]Zr-DFO-Bn-NCS Vs [^{89}Zr]Zr-Hy$_3$ADA^5-NCS; $^{\#}p < 0.05$ WBCs labeled with [^{89}Zr]Zr-DFO-Bn-NCS Vs [^{89}Zr]Zr-Hy$_3$ADA^5-SA and $^{¶}p < 0.05$ WBCs labeled with [^{89}Zr]Zr-Hy$_3$ADA^5-NCS Vs [^{89}Zr]Zr-Hy$_3$ADA^5-SA.

of [^{89}Zr]Zr-WBCs radiolabeled with [^{89}Zr]Zr-DFO-Bn-NCS. For WBCs radiolabeled with [^{89}Zr]Zr-Hy$_3$ADA^5-NCS, significant localization of radioactivity was found in liver, spleen and intestine, a similar trend in distribution of radiolabeled WBCs as observed with [^{89}Zr]Zr-DFO-Bn-NCS. Additionally, WBCs radiolabeled with [^{89}Zr]Zr-Hy$_3$ADA^5-SA also showed primarily similar uptake in liver and spleen but increased uptake in bone over time suggesting instability of [^{89}Zr]Zr-Hy$_3$ADA^5-SA conjugation with surface proteins or in vivo demetallation of ^{89}Zr from [^{89}Zr]Zr-Hy$_3$ADA^5-SA conjugate.

Overall, the in vivo stability of [^{89}Zr]Zr-DFO-Bn-NCS as demonstrated here is promising and superior over other synthons [^{89}Zr]Zr-Hy$_3$ADA^5-NCS and [^{89}Zr]Zr-Hy$_3$ADA^5-SA. Of these, [^{89}Zr]Zr-Hy$_3$ADA^5-SA showed the lowest in-vivo stability but had considerably higher in vitro stability[66]. The biodistribution of radiolabeled WBCs in the rest of the major organs are presented in Figs. 6 and 7 and Table 2, indicating mild uptake in lung, heart, muscle, pancreas, and skin at 7 days post injection.

Small animal PET imaging and biodistribution of ^{89}Zr labeled SCs. Small animal PET imaging and biodistribution of SCs were performed independently after radiolabeling of SCs with three different radiolabeling synthons, [^{89}Zr]Zr-DFO-Bn-NCS, [^{89}Zr]Zr-Hy$_3$ADA^5-NCS, and [^{89}Zr]Zr-Hy$_3$ADA^5-SA to assess any variation in pharmacokinetics of SCs radiolabeled with different synthons in healthy athymic mice (Fig. 8). The SCs radiolabeled with ^{89}Zr using [^{89}Zr]Zr-DFO-Bn-NCS and [^{89}Zr]Zr-Hy$_3$ADA^5-NCS showed uptake primarily in lung, liver and spleen at all time points with some early uptake in intestine. The SCs radiolabeled with [^{89}Zr]Zr-

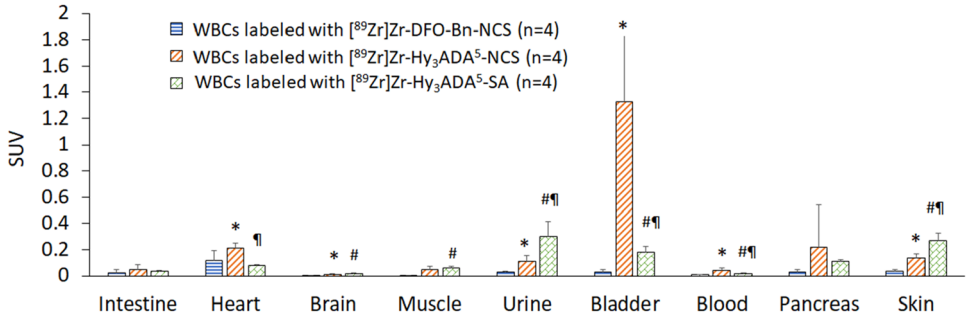

Figure 7. Uptake (SUV) and biodistribution of WBCs labeled with [^{89}Zr]Zr-DFO-NCS, [^{89}Zr]Zr-Hy$_3$ADA^5-NCS and [^{89}Zr]Zr-Hy$_3$ADA^5-SA synthons in athymic nude mice at day 7 post-injection. *$p < 0.05$ WBCs labeled with [^{89}Zr]Zr-DFO-Bn-NCS Vs [^{89}Zr]Zr-Hy$_3$ADA^5-NCS; $^{\#}p < 0.05$ WBCs labeled with [^{89}Zr]Zr-DFO-Bn-NCS Vs [^{89}Zr]Zr-Hy$_3$ADA^5-SA and ¶$p < 0.05$ WBCs labeled with [^{89}Zr]Zr-Hy$_3$ADA^5-NCS Vs [^{89}Zr]Zr-Hy$_3$ADA^5-SA.

Organ	White blood cells labeled with		
	[^{89}Zr]Zr-DFO-Bn-NCS SUV average ± SD	[^{89}Zr]Zr-Hy3ADA5-NCS SUV average ± SD	[^{89}Zr]Zr-Hy3ADA5-SA SUV average ± SD
Lung	0.68 ± 0.26	1.32 ± 1.32	0.25 ± 0.056$^{\#}$
Liver	16.67 ± 1.05	11.12 ± 2.11*	10.08 ± 0.99$^{\#}$
Spleen	24.34 ± 4.30	7.69 ± 1.44	7.74 ± 2.10
Kidney	0.19 ± 0.75	0.76 ± 0.060*	0.37 ± 0.10$^{\#}$
Bones	0.83 ± 0.56	0.99 ± 0.42	4.70 ± 1.41$^{\#¶}$
Intestine	0.02 ± 0.02	0.046 ± 0.042	0.037 ± 0.006
Heart	0.12 ± 0.07	0.21 ± 0.038*	0.08 ± 0.003
Brain	0.003 ± 0.001	0.011 ± 0.006*	0.015 ± 0.0096$^{\#}$
Muscle	0.020 ± 0.027	0.049 ± 0.026	0.063 ± 0.0081$^{\#}$
Urine	0.030 ± 0.0044	0.11 ± 0.049*	0.30 ± 0.12$^{\#¶}$
Bladder	0.030 ± 0.017	1.33 ± 0.51*	0.18 ± 0.05$^{\#¶}$
Blood	0.0098 ± 0.0030	0.044 ± 0.019*	0.019 ± 0.006$^{\#¶}$
Pancreas	0.027 ± 0.023	0.22±0.32	0.11 ± 0.02$^{\#}$
Skin	0.036 ± 0.015	0.14 ± 0.034*	0.27 ± 0.05$^{\#¶}$

Table 2. Uptake (SUV) and biodistribution of white blood cells (WBCs) labeled with [^{89}Zr]Zr-DFO-NCS (n = 4), [^{89}Zr]Zr-Hy$_3$ADA^5-NCS (n = 4) and [^{89}Zr]Zr-Hy$_3$ADA^5-SA (n = 4) synthons in athymic nude mice at day 7 post-injection. *$p < 0.05$ WBCs labeled with [^{89}Zr]Zr-DFO-Bn-NCS Vs [^{89}Zr]Zr-Hy$_3$ADA^5-NCS. $^{\#}p < 0.05$ WBCs labeled with [^{89}Zr]Zr-DFO-Bn-NCS Vs [^{89}Zr]Zr-Hy$_3$ADA^5-SA. ¶$p < 0.05$ WBCs labeled with [^{89}Zr]Zr-Hy$_3$ADA^5-NCS Vs [^{89}Zr]Zr-Hy$_3$ADA^5-SA.

Hy$_3$ADA^5-NCS showed some localization of radioactivity in lung, liver, spleen and intestine but had prominent accumulation of radioactivity in bones at day 2 post-injection. The detection of radioactivity signals in bone of SCs radiolabeled with [^{89}Zr]Zr-Hy$_3$ADA^5-NCS but not with [^{89}Zr]Zr-DFO-Bn-NCS suggested in vivo instability of [^{89}Zr]Zr-Hy$_3$ADA^5-NCS conjugate with surface proteins. Interestingly, the small animal PET imaging of SCs radiolabeled with [^{89}Zr]Zr-Hy$_3$ADA^5-SA showed most of the radioactivity in lungs at all time points, whereas the radioactivity in bones significantly increased from day 2 onwards. The significant increase in radioactivity accumulation in bone further suggested in vivo instability of [^{89}Zr]Zr-Hy$_3$ADA^5-SA. Overall, synthon [^{89}Zr]Zr-DFO-Bn-NCS was found to be a superior performer in stem cell radiolabeling and tracking over time as compared to [^{89}Zr]Zr-Hy$_3$ADA^5-NCS and [^{89}Zr]Zr-Hy$_3$ADA^5-SA. The biodistribution of radiolabeled SCs in the rest of the major organs are presented in Figs. 9 and 10 and Table 3, indicating mild uptake in lung, heart, kidney, muscle, pancreas, and skin at 7 days post injection.

Small animal PET imaging of un-chelated [^{89}Zr]ZrCl$_4$. The in vivo characteristics of un-chelated [^{89}Zr]ZrCl$_4$ was also investigated (Fig. 11). The small animal PET imaging showed a high accumulation of free ^{89}Zr in the bones at 4 h and did not distribute to the lung, liver, spleen, or any other organs at any other time points as were noted with radiolabeled WBCs and SCs. The radioactivity increased significantly on day 2 and remained in the bones until day 7, attributed to the entrapment of osteophilic ^{89}Zr and its poor clearance from the bones (Fig. 12, Table 4). This observation is consistent with findings by Abou et al. 2011 demonstrating that [^{89}Zr]ZrCl$_4$ is a bone-seeking species and accumulates in bones and joints post-administration in mice[71].

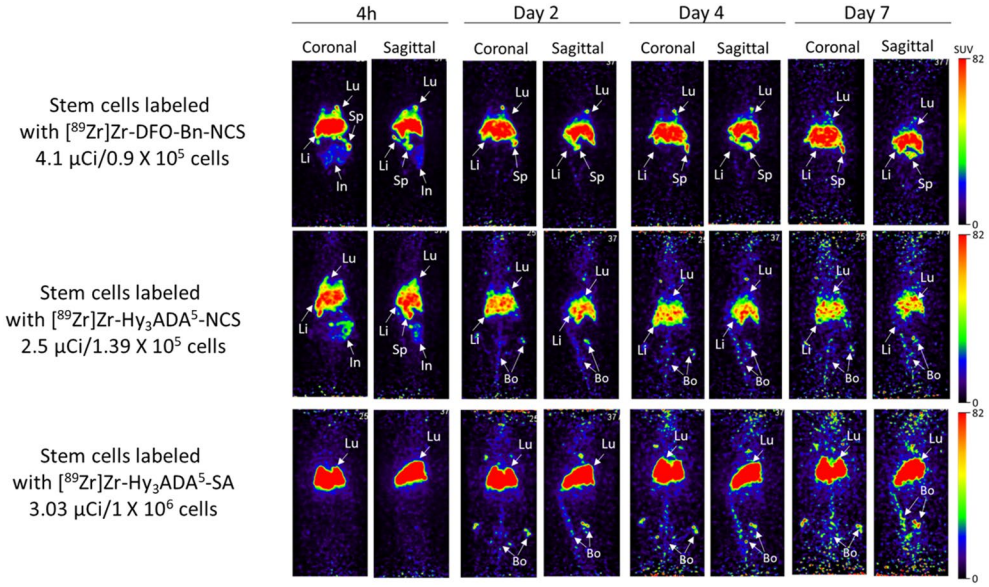

Figure 8. Representative coronal and sagittal PET maximum intensity projection (MIP) images showing distribution of stem cells labeled with [^{89}Zr]Zr-DFO-NCS, [^{89}Zr]Zr-Hy$_3$ADA^5-NCS and [^{89}Zr]Zr-Hy$_3$ADA^5-SA synthons in athymic nude mice at different time points post-injection.

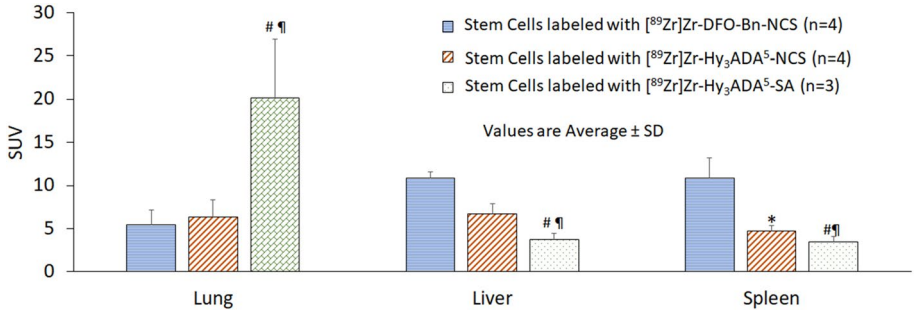

Figure 9. Uptake (SUV) and biodistribution of stem cells labeled with [^{89}Zr]Zr-DFO-NCS, [^{89}Zr]Zr-Hy$_3$ADA^5-NCS and [^{89}Zr]Zr-Hy$_3$ADA^5-SA synthons in lung, liver and spleen of athymic nude mice at day 7 post-injection. *$p < 0.05$ stem cells labeled with [^{89}Zr]Zr-DFO-Bn-NCS Vs with [^{89}Zr]Zr-Hy$_3$ADA^5-NCS; #$p < 0.05$ stem cells labeled with [^{89}Zr]Zr-DFO-Bn-NCS Vs [^{89}Zr]Zr-Hy$_3$ADA^5-SA and ¶$p < 0.05$ stem cells labeled with [^{89}Zr]Zr-Hy$_3$ADA^5-NCS Vs [^{89}Zr]Zr-Hy$_3$ADA^5-SA.

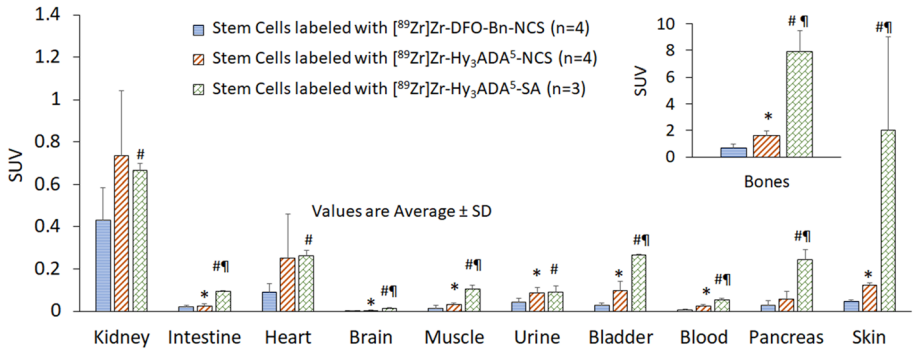

Figure 10. Uptake (SUV) and biodistribution of stem cells labeled with [^{89}Zr]Zr-DFO-NCS, [^{89}Zr]Zr-Hy$_3$ADA^5-NCS and [^{89}Zr]Zr-Hy$_3$ADA^5-SA synthons in athymic nude mice at day 7 post-injection. *$p < 0.05$ stem cells labeled with [^{89}Zr]Zr-DFO-Bn-NCS Vs [^{89}Zr]Zr-Hy$_3$ADA^5-NCS; #$p < 0.05$ stem cells labeled with [^{89}Zr]Zr-DFO-Bn-NCS Vs [^{89}Zr]Zr-Hy$_3$ADA^5-SA and ¶$p < 0.05$ stem cells labeled with [^{89}Zr]Zr-Hy$_3$ADA^5-NCS Vs [^{89}Zr]Zr-Hy$_3$ADA^5-SA.

Organ	Stem cells labeled with		
	[^{89}Zr]Zr-DFO-Bn-NCS	[^{89}Zr]Zr-Hy$_3$ADA^5-NCS	[^{89}Zr]Zr-Hy$_3$ADA^5-SA
	SUV average ± SD	SUV average ± SD	SUV average ± SD
Lung	5.44 ± 1.72	6.35 ± 1.98	20.15 ± 6.79$^{\#¶}$
Liver	10.88 ± 0.72	6.75 ± 1.17	3.73 ± 0.69$^{\#¶}$
Spleen	10.88 ± 2.37	4.69 ± 0.69*	3.44 ± 0.61$^{\#¶}$
Kidney	0.43 ± 0.15	0.74 ± 0.30	0.67 ± 0.03$^{\#}$
Bones	0.68 ± 0.27	1.61 ± 0.36*	7.91 ± 1.55$^{\#¶}$
Intestine	0.022 ± 0.006	0.024 ± 0.010	0.09 ± 0.004
Heart	0.09 ± 0.04	0.25 ± 0.21	0.26 ± 0.02
Brain	0.002 ± 0.001	0.004 ± 0.001	0.012 ± 0.004$^{\#}$
Muscle	0.014 ± 0.013	0.033 ± 0.005*	0.11 ± 0.018$^{\#¶}$
Urine	0.044 ± 0.018	0.086 ± 0.024*	0.092 ± 0.028$^{\#¶}$
Bladder	0.029 ± 0.01	0.099 ± 0.041*	0.27 ± 0.002$^{\#¶}$
Blood	0.0072 ± 0.0025	0.02 ± 0.006*	0.055 ± 0.006$^{\#¶}$
Pancreas	0.029 ± 0.020	0.058 ± 0.036	0.24 ± 0.048¶
Skin	0.047 ± 0.006	0.12 ± 0.013*	0.86 ± 0.44$^{\#¶}$

Table 3. Uptake (SUV) and biodistribution of stem cells labeled with [^{89}Zr]Zr-DFO-NCS (n = 4) , [^{89}Zr]Zr-Hy$_3$ADA^5-NCS (n = 4) and [^{89}Zr]Zr-Hy$_3$ADA^5-SA (n = 3) synthons in athymic nude mice at day 7 post-injection. *$p < 0.05$ stem cells labeled with [^{89}Zr]Zr-DFO-Bn-NCS Vs [^{89}Zr]Zr-Hy$_3$ADA^5-NCS; $^{\#}p < 0.05$ stem cells labeled with [^{89}Zr]Zr-DFO-Bn-NCS Vs [^{89}Zr]Zr-Hy$_3$ADA^5-SA and $^{¶}p < 0.05$ stem cells labeled with [^{89}Zr]Zr-Hy$_3$ADA^5-NCS Vs [^{89}Zr]Zr-Hy$_3$ADA^5-SA.

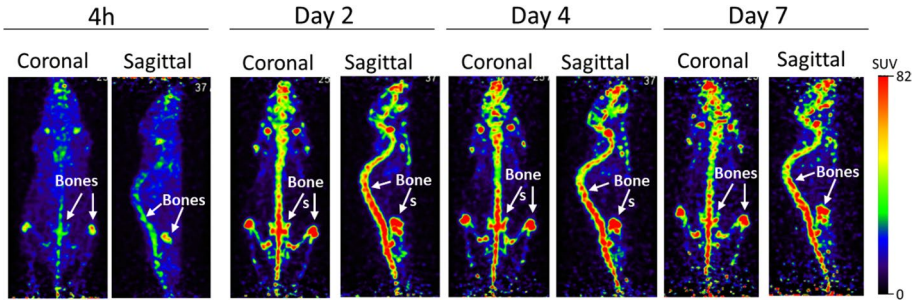

Figure 11. Representative coronal and sagittal PET maximum intensity projection (MIP) images showing distribution of [^{89}Zr]ZrCl$_4$ in athymic nude mice at different time points post-injection.

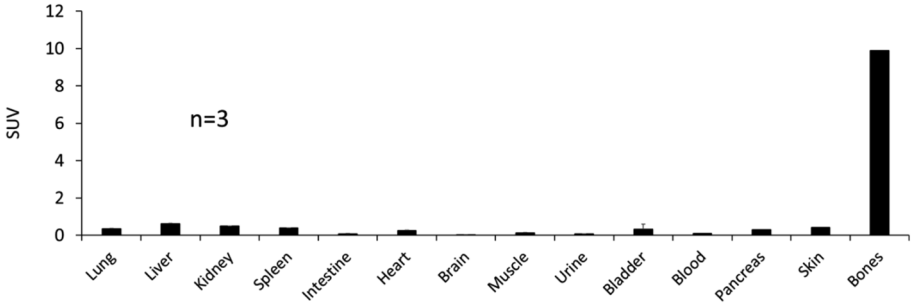

Figure 12. Uptake (SUV) and distribution of [^{89}Zr]ZrCl$_4$ in athymic nude mice at day 7 post-injection.

Conclusion

Both WBCs and SCs were successfully directly radiolabeled with ^{89}Zr using three different ready-to-use synthons, [^{89}Zr]Zr-DFO-Bn-NCS, [^{89}Zr]Zr-Hy$_3$ADA^5-NCS and [^{89}Zr]Zr-Hy$_3$ADA^5-SA. The radiolabeling efficiencies of cells (WBCs and SCs) were significantly higher with [^{89}Zr]Zr-DFO-Bn-NCS than ^{89}Zr]Zr-Hy$_3$ADA^5-NCS and [^{89}Zr]Zr-Hy$_3$ADA^5-SA. The higher cell radiolabeling efficiency with [^{89}Zr]Zr-DFO-Bn-NCS could be attributed to an open chain structure of DFO. In vivo, the stability of ^{89}Zr complexed with DFO and Hy$_3$ADA^5 chelators were

Free Zr-89	SUV average ± SD
Lung	0.36 ± 0.06
Liver	0.61 ± 0.07
Kidney	0.49 ± 0.07
Spleen	0.39 ± 0.09
Intestine	0.09 ± 0.01
Heart	0.26 ± 0.03
Brain	0.02 ± 0.02
Muscle	0.14 ± 0.05
Urine	0.08 ± 0.03
Bladder	0.32 ± 0.09
Blood	0.12 ± 0.01
Pancreas	0.29 ± 0.02
Skin	0.42 ± 0.14
Bones	9.89 ± 0.4

Table 4. Uptake (SUV) and distribution of [^{89}Zr]$ZrCl_4$ in athymic nude mice (n = 3) at day 7 post-injection.

found to be comparable. The synthons [^{89}Zr]Zr-DFO-Bn-NCS, and [^{89}Zr]Zr-Hy_3ADA^5-NCS could be considered to radiolabel cells for further application; synthon [^{89}Zr]Zr-Hy_3ADA^5-SA showed higher bone uptake indicating its poor stability (synthon-protein conjugation) in vivo. Further optimization of the [^{89}Zr]Zr-Hy_3ADA^5-SA synthon is needed to enhance cell radiolabeling efficiency and stability. Overall, the PET-based cell radiolabeling methodology offers an effective tool to noninvasively track WBCs, SCs, and other cells to understand the safety, efficacy, distribution, and clearance of cell-based therapies.

Materials and methods

General. The ^{89}Zr used in this study was produced on a PETtrace cyclotron (GE Healthcare, Waukesha, WI) using ^{89}Y target foil (0.1 mm; 50 X 50 mm, 99.9%), which was purchased from Alfa-Aesar, Haverhill, MA. The trace metal grade nitric acid (67–70%) and hydrochloric acid (34–37%) were purchased from Thermo Fisher Scientific, Waltham, MA. Sodium bicarbonate, oxalic acid dehydrate (*Trace*SELECT® ≥ 99.9999% metal basis), sodium carbonate, sodium citrate dihydrate and HPLC grade acetonitrile were purchased from Sigma Aldrich, St. Louis, MO. The silica gel iTLC was purchased from Agilent Technologies, Santa Clara, CA. The chelator p-SCN-Bn-Deferoxamine or DFO-Bn-NCS (≥ 94%) was purchased from Macrocylics, Plano, TX, whereas the other two chelators Hy_3ADA^5-NCS and Hy_3ADA^5-SA were synthesized as described by Klasen et al.[66]. The empty Luer-Inlet SPE cartridges (1 mL) with frits (20 µm pore size) were purchased from Supelco Inc (Bellefonte, PA) and Chromafix® 30-PS-HCO_3 PP cartridges (45 mg) were purchased from Macherey–Nagel, Duren, Germany. The Millex®-GV filter (0.2 µm) was purchased from Millipore Sigma, Burlington, MA. The hydroxamate resin was synthesized in-house as demonstrated by Pandey et al.[67–70] The Thermomixer was purchased from Eppendorf, Hamburg, Germany.

Production and purification of [^{89}Zr]$ZrCl_4$. The ^{89}Zr was produced using yttrium foil on a solid target through a ^{89}Y(p,n)^{89}Zr nuclear reaction in a PETtrace cyclotron as described previously by Pandey et al.[68]. ^{89}Zr was purified first as [^{89}Zr]Zr-oxalate and then converted to [^{89}Zr]$ZrCl_4$ using activated Chromafix 30-PS-HCO_3 SPE as demonstrated by Pandey[67–70] and Larenkov et al.[72], respectively. The final [^{89}Zr]$ZrCl_4$ was eluted in ~ 0.5 mL of 1.0 N HCl and then dried using a steady flow of nitrogen gas in a V-vial at 65 °C.

Apparent molar activity of [^{89}Zr]$ZrCl_4$. The apparent molar activity of ^{89}Zr was estimated using a DFO-Bn-NCS titration method. In this method, 10µL [^{89}Zr]$ZrCl_4$ (36.4 MBq) was added to 90µL de-ionized H_2O. To this, 4 µL of 0.5 M Na_2CO_3 was added to neutralize and adjust the pH to 7.5–8.0. To the neutralized mixture, 0.01–10 µg of DFO-Bn-NCS in 4µL of DMSO was added and mixed. The complexation mixture was then incubated at 37 °C for 1 h. After 1 h, the degree of ^{89}Zr complexation was determined with respect to the DFO-Bn-NCS concentration using radio-TLC with 20 mM sodium citrate (pH 4.9–5.1) as a mobile phase. The complexed ^{89}Zr as [^{89}Zr]Zr-DFO-Bn-NCS showed at the origin with $R_f = 0$, whereas free or un-complexed ^{89}Zr had an R_f of 0.99 (solvent front). The half maximal inhibitory concentration (IC_{50}) of DFO-Bn-NCS in mg/mL was calculated using non-linear regression curve fitting analysis.

The analysis was performed using analysis software—GraphPad Prism 9 (GraphPad Software, San Diego, CA). The minimum ligand concentration for which 100% complexation occurred was estimated by multiplying the IC_{50} by 2, and the apparent molar activity (GBq/µmole) and the apparent specific activity (GBq/mg) of ^{89}Zr were calculated by correcting for the total activity divided by µmoles or mg of DFO-Bn-NCS needed for 100% ^{89}Zr complexation.

Radiosynthesis of [^{89}Zr]Zr-DFO-Bn-NCS, [^{89}Zr]Zr-Hy_3ADA^5-NCS and [^{89}Zr]Zr-Hy_3ADA^5-SA. The radiosynthesis of the different synthons [^{89}Zr]Zr-DFO-Bn-NCS, [^{89}Zr]Zr-Hy_3ADA^5-

NCS and [^{89}Zr]Zr-Hy$_3$ADA^5-SA were performed using a modified procedure demonstrated in our previous work.[58] The purified [^{89}Zr]ZrCl$_4$ was resuspended in appropriate volume of 0.1 N HCl and then neutralized to pH ~ 8.0 with 0.5 M Na_2CO_3. The neutralized [^{89}Zr]ZrCl$_4$ solution (70 -100 µL) containing ~ 21 MBq of ^{89}Zr was used in the case of DFO-Bn-NCS, whereas ~ 61 to 68 MBq of ^{89}Zr was used in the case of Hy$_3$ADA^5-NCS and Hy$_3$ADA^5-SA. To this neutralized [^{89}Zr]ZrCl$_4$ solution, 4 nmoles of DFO-Bn-NCS or Hy$_3$ADA^5-NCS or Hy$_3$ADA^5-SA (prepared in DMSO) were added in separate reactions. The resultant reaction mixtures were stirred for 30 min at 37 °C in a thermomixer at 500 rpm. The radiolabeling efficiency was determined at different time points by silica radio-TLC using 20 mM sodium citrate (pH 4.9–5.1) as a mobile phase.

Cell preparation. The human mesenchymal SCs were gifted by Dr. Atta Behfar from the Department of Cardiovascular Medicine, Mayo Clinic, Rochester, MN, USA, and WBCs were isolated from the peripheral blood provided by the Division of Transfusion Medicine, Mayo Clinic, Rochester, MN, USA. The isolation of WBCs from the peripheral blood was performed using Lymphoprep™ (STEMCELL Technologies Inc., Canada) gradient centrifugation method as per manufacturer instructions. The final WBC solution was washed with Hank's Balanced Salt Solution.

Cell radiolabeling. The SCs and WBCs cells were radiolabeled with different synthons, [^{89}Zr]Zr-DFO-Bn-NCS, [^{89}Zr]Zr-Hy$_3$ADA^5-NCS and [^{89}Zr]Zr-Hy$_3$ADA^5-SA separately. The cell radiolabeling mixture was prepared by mixing equal volume of the [^{89}Zr]Zr-DFO-Bn-NCS or [^{89}Zr]Zr-Hy^{3}ADA^5-NCS or [^{89}Zr]Zr-Hy$_3$ADA^5-SA reaction mix and equal volume of phosphate buffer-HEPES. The phosphate buffer-HEPES was prepared by mixing 120 µL of 1.2 M phosphate buffer and 100 µL of 1 M HEPES. This cell radiolabeling mix was incubated at room temperature for 30 min. As a negative control, a cell radiolabeling mix with [^{89}Zr]ZrCl$_4$ was also tested for radiolabeling SCs and WBCs. After this incubation, the cell radiolabeling mixture (~ 150 to 200 µL) was added to a cell suspension at a concentration of 6×10^6 cells in 500 µL HEPES Buffered Hank's Balanced Salt Solution at pH 7.5–8.0[58,59]. The cell radiolabeling was performed for 30 min at room temperature for WBCs and 37 °C for SCs in a thermomixer. After radiolabeling, the cells were washed 3× with complete Dulbecco's Modified Eagle Medium.

Trypan blue exclusion assay cellular viability test. The effect of radiolabeling on cellular viability was assessed using the trypan blue exclusion assay test within 1 h of labeling.

Animals. 8–10 week old athymic nude mice (male and female, 1:1) were obtained from Charles Rivers Laboratories or Taconic Biosciences, Inc.

PET imaging and ex vivo biodistribution studies. After radiolabeling, the radiolabeled WBCs (0.1–0.6×10^6; 0.03–0.11 MBq); and SCs ($0.1–1 \times 10^6$; 0.1–0.15 MBq) were injected via tail vein into a group (n = 3) of athymic nude mice. PET images were acquired at 4 h, 2 days, 4 days and 7 days post-injection (p.i.) using a small animal PET scanner. The free [^{89}Zr]ZrCl$_4$ with radioactivity (0.15–0.19 MBq) was also injected intravenously via the tail vein. The small animal PET images were visualized, analyzed, and scaled to SUV using image analysis software, MIM 7 software (MIM Software Inc., Cleveland, OH, USA). The PET images are shown as maximum intensity projection (MIP) images in the coronal and sagittal plane. The animals were euthanized at 7d p.i., and organs/tissues collected to measure the standardized uptake value (SUV) in major organs. Animals were euthanized via cardiectomy under anesthesia using isoflurane as approved by the Institutional Animal Care and Use Committee (IACUC) of the Mayo Clinic Rochester MN USA. SUV was calculated using following formula:

$$Standardized\ Uptake\ Value = \frac{Radioactivity\ concentration\ in\ tissue\ (\mu Ci/g)}{\frac{Injected\ dose\ (\mu Ci)}{Body\ Weight(g)}}$$

Statistics. The obtained data were analyzed using Microsoft Excel program and the results were compared using unpaired Student's t-test analysis. Differences were regarded as statistically significant for $p < 0.05$.

Ethical standards. Studies were conducted with proper use and care of animals as approved by the Institutional Animal Care and Use Committee of the Mayo Clinic Rochester MN USA. Additionally, all methods were also performed in accordance with Institutional Animal Care and Use Committee's guidelines and regulation. These guidelines are equivalent to the ARRIVE guidelines and therefore all methods were also performed in accordance with ARRIVE guidelines.

Data availability

All data generated or analyzed during this study are included in this published article.

Received: 20 May 2022; Accepted: 7 September 2022
Published online: 19 September 2022

References

1. Noh, Y. W., Lim, Y. T. & Chung, B. H. Noninvasive imaging of dendritic cell migration into lymph nodes using near-infrared fluorescent semiconductor nanocrystals. *FASEB J.* **22**, 3908–3918 (2008).

2. Yukawa, H. & Baba, Y. In vivo fluorescence imaging and the diagnosis of stem cells using quantum dots for regenerative medicine. *Anal. Chem.* **89**, 2671–2681 (2017).
3. Ren, P. G., Lee, S. W., Biswal, S. & Goodman, S. B. Systemic trafficking of macrophages induced by bone cement particles in nude mice. *Biomaterials* **29**, 4760–4765 (2008).
4. Han, D. & Wu, J. C. Using bioengineered bioluminescence to track stem cell transplantation in vivo. *Methods Mol. Biol.* **2126**, 1–11 (2020).
5. Liu, W.-W. & Li, P.-C. Photoacoustic imaging of cells in a three-dimensional microenvironment. *J. Biomed. Sci.* **27**, 3 (2020).
6. James, S., Neuhaus, K., Murphy, M. & Leahy, M. Contrast agents for photoacoustic imaging: A review of stem cell tracking. *Stem Cell Res. Ther.* **12**, 511 (2021).
7. Kim, T., Lemaster, J. E., Chen, F., Li, J. & Jokerst, J. V. Photoacoustic imaging of human mesenchymal stem cells labeled with Prussian Blue-poly(L-lysine) nanocomplexes. *ACS Nano* **11**, 9022–9032 (2017).
8. Ahrens, E. T. & Bulte, J. W. M. Tracking immune cells in vivo using magnetic resonance imaging. *Nat. Rev. Immunol.* **13**, 755–763 (2013).
9. Valable, S. *et al.* In vivo MRI tracking of exogenous monocytes/macrophages targeting brain tumors in a rat model of glioma. *Neuroimage* **40**, 973–983 (2008).
10. Neuwelt, A. *et al.* Iron-based superparamagnetic nanoparticle contrast agents for MRI of infection and inflammation. *AJR Am. J. Roentgenol.* **204**, W302-313 (2015).
11. Huang, J., Bao, H., Li, X. & Zhang, Z. In vivo CT imaging tracking of stem cells labeled with Au nanoparticles. *View.* **3**, 20200119 (2022).
12. Yu, C. *et al.* Enhanced and long-term CT imaging tracking of transplanted stem cells labeled with temperature-responsive gold nanoparticles. *J. Mater. Chem. B.* **9**, 2854–2865 (2021).
13. Kim, T. *et al.* In vivo micro-CT imaging of human mesenchymal stem cells labeled with gold-poly-L-lysine nanocomplexes. *Adv. Funct. Mater.* **27**, 1604213 (2017).
14. Nose, N. *et al.* [^{18}F]FDG-labelled stem cell PET imaging in different route of administrations and multiple animal species. *Sci. Rep.* **11**, 10896 (2021).
15. Wei, W., Jiang, D., Ehlerding, E. B., Luo, Q. & Cai, W. Noninvasive PET imaging of T cells. *Trends Cancer.* **4**, 359–373 (2018).
16. McCracken, M. N., Tavaré, R., Witte, O. N. & Wu, A. M. Advances in PET detection of the antitumor T cell response. *Adv. Immunol.* **131**, 187–231 (2016).
17. Zhang, Y. *et al.* Tracking stem cell therapy in the myocardium: Applications of positron emission tomography. *Curr. Pharm. Des.* **14**, 3835–3853 (2008).
18. Fu, Y. *et al.* PET-MRI tracking of imaging-visible microencapsulated stem cells in immunocompetent rabbits. *J. Cardiovasc. Magn. Reson.* **15**, M1 (2013).
19. Galli, F. *et al.* In vivo imaging of natural killer cell trafficking in tumors. *J. Nucl. Med.* **56**, 1575–1580 (2015).
20. Cheng, S.-H. *et al.* Dynamic in vivo SPECT imaging of neural stem cells functionalized with radiolabeled nanoparticles for tracking of glioblastoma. *J. Nucl. Med.* **57**, 279–284 (2016).
21. Yang, X. *et al.* Cellular and molecular imaging for stem cell tracking in neurological diseases. *Stroke Vasc. Neurol.* **6**, 121–127 (2021).
22. Zheng, Y. *et al.* Stem cell tracking technologies for neurological regenerative medicine purposes. *Stem Cells Int.* **2017**, 2934149–2934149 (2017).
23. Lechermann, L. M., Lau, D., Attili, B., Aloj, L. & Gallagher, F. A. In vivo cell tracking using PET: Opportunities and challenges for clinical translation in oncology. *Cancers (Basel)* **13**, 4042 (2021).
24. Stanton, S. E. *et al.* Concurrent SPECT/PET-CT imaging as a method for tracking adoptively transferred T-cells in vivo. *J. Immunother. Cancer.* **4**, 27 (2016).
25. Manley, N. C. & Steinberg, G. K. Tracking stem cells for cellular therapy in stroke. *Curr. Pharm. Des.* **18**, 3685–3693 (2012).
26. Lee, S. B. *et al.* Tracking dendritic cell migration into lymph nodes by using a novel PET probe ^{18}F-tetrafluoroborate for sodium/iodide symporter. *EJNMMI Res.* **7**, 32–32 (2017).
27. Socan, A., Sever, M., Vrtovec, B. & Lezaic, L. Evaluation of CD34+ HPCs labeled with ^{99m}Tc-HMPAO. *J. Nucl. Med.* **54**, 1665–1665 (2013).
28. Peters, A. M. *et al.* Clinical experience with ^{99m}Tc-hexamethylpropylene-amineoxime for labelling leucocytes and imaging inflammation. *Lancet* **2**, 946–949 (1986).
29. Dudhia, J. *et al.* In vivo imaging and tracking of Technetium-99m labeled bone marrow mesenchymal stem cells in equine tendinopathy. *J. Vis. Exp.* **106**, 52748 (2015).
30. Thakur, M. L. *et al.* Indium-111-labeled cellular blood components: Mechanism of labeling and intracellular location in human neutrophils. *J. Nucl. Med.* **18**, 1022–1026 (1977).
31. Gholamrezanezhad, A. *et al.* In vivo tracking of ^{111}In-oxine labeled mesenchymal stem cells following infusion in patients with advanced cirrhosis. *Nucl. Med. Biol.* **38**, 961–967 (2011).
32. Ullman, H., Viragh, K., Thomas, M. & Ni, C. ^{111}In-labeled white blood cell uptake in the urinary bladder in occult urinary tract infection. *Clin. Nucl. Med.* **46**, 159–160 (2021).
33. Hughes, D. K. Nuclear medicine and infection detection: the relative effectiveness of imaging with ^{111}In-oxine-, ^{99m}Tc-HMPAO-, and ^{99m}Tc-stannous fluoride colloid-labeled leukocytes and with ^{67}Ga-citrate. *J. Nucl. Med. Technol.* **31**, 196–201 (2003) (**quiz 203-194**).
34. Jung, K. O. *et al.* Whole-body tracking of single cells via positron emission tomography. *Nat. Biomed. Eng.* **4**, 835–844 (2020).
35. Stojanov, K. *et al.* [^{18}F]FDG labeling of neural stem cells for in vivo cell tracking with positron emission tomography: Inhibition of tracer release by phloretin. *Mol. Imaging.* **11**, 1–12 (2012).
36. Adonai, N. *et al.* Ex vivo cell labeling with ^{64}Cu–pyruvaldehyde-bis(N4-methylthiosemicarbazone) for imaging cell trafficking in mice with positron-emission tomography. *Proc. Natl. Acad. Sci. USA* **99**, 3030–3035 (2002).
37. Welch, M. J. *et al.* Gallium-68 labeled red cells and platelets: New agents for positron tomography. *J. Nucl. Med.* **18**, 558–562 (1977).
38. Thompson, S. *et al.* Automated synthesis of [^{68}Ga]oxine, improved preparation of ^{68}Ga-labeled erythrocytes for blood-pool imaging, and preclinical evaluation in rodents. *Medchemcomm.* **9**, 454–459 (2018).
39. Sato, N. *et al.* ^{89}Zr-oxine complex PET cell imaging in monitoring cell-based therapies. *Radiology* **275**, 490–500 (2015).
40. Man, F. *et al.* In vivo PET tracking of ^{89}Zr-labeled Vgamma9Vdelta2 T cells to mouse xenograft breast tumors activated with liposomal alendronate. *Mol. Ther.* **27**, 219–229 (2019).
41. Nagengast, W. B. *et al.* In vivo VEGF imaging with radiolabeled bevacizumab in a human ovarian tumor xenograft. *J. Nucl. Med.* **48**, 1313–1319 (2007).
42. Oude Munnink, T. H. *et al.* ^{89}Zr-trastuzumab PET visualises HER2 downregulation by the HSP90 inhibitor NVP-AUY922 in a human tumour xenograft. *Eur. J. Cancer.* **46**, 678–684 (2010).
43. Jacobson, O. *et al.* MicroPET imaging of integrin αvβ3 expressing tumors using ^{89}Zr-RGD peptides. *Mol. Imaging Biol.* **13**, 1224–1233 (2011).
44. Evans, M. J. *et al.* Imaging tumor burden in the brain with ^{89}Zr-transferrin. *J. Nucl. Med.* **54**, 90–95 (2013).
45. Keliher, E. J. *et al.* ^{89}Zr-labeled dextran nanoparticles allow in vivo macrophage imaging. *Bioconjug. Chem.* **22**, 2383–2389 (2011).
46. Wilks, M. *et al.* In vivo PET imaging of T-cell trafficking by ^{89}Zr-radiolabeled nanoparticles. *J. Nucl. Med.* **58**, 622–622 (2017).

47. Fairclough, M. *et al.* A new technique for the radiolabelling of mixed leukocytes with zirconium-89 for inflammation imaging with positron emission tomography. *J. Label. Comp. Radiopharm.* **59**, 270–276 (2016).
48. Ferris, T. J. *et al.* Synthesis and characterisation of zirconium complexes for cell tracking with Zr-89 by positron emission tomography. *Dalton Trans.* **43**, 14851–14857 (2014).
49. Charoenphun, P. *et al.* [^{89}Zr](oxinate)$_4$ for long-term in vivo cell tracking by positron emission tomography. *Eur. J. Nucl. Med. Mol. Imaging.* **42**, 278–287 (2015).
50. Asiedu, K. O., Koyasu, S., Szajek, L. P., Choyke, P. L. & Sato, N. Bone marrow cell trafficking analyzed by ^{89}Zr-oxine positron emission tomography in a murine transplantation model. *Clin. Cancer Res.* **23**, 2759 (2017).
51. Asiedu, K. O. *et al.* Bone marrow cell homing to sites of acute tibial fracture: ^{89}Zr-oxine cell labeling with positron emission tomographic imaging in a mouse model. *EJNMMI Res.* **8**, 109 (2018).
52. Weist, M. R. *et al.* PET of adoptively transferred chimeric antigen receptor T cells with ^{89}Zr-oxine. *J. Nucl. Med.* **59**, 1531–1537 (2018).
53. Sato, N. *et al.* In vivo tracking of adoptively transferred natural killer cells in rhesus macaques using ^{89}Zirconium-oxine cell labeling and PET imaging. *Clin. Cancer Res.* **26**, 2573–2581 (2020).
54. Man, F., Khan, A. A., Carrascal-Minino, A., Blower, P. J. & de Rosales, R. T. M. A kit formulation for the preparation of [^{89}Zr]Zr(oxinate)$_4$ for PET cell tracking: White blood cell labelling and comparison with [^{111}In]In(oxinate)$_3$. *Nucl. Med. Biol.* **90–91**, 31–40 (2020).
55. Patrick, P. S. *et al.* Lung delivery of MSCs expressing anti-cancer protein TRAIL visualised with ^{89}Zr-oxine PET-CT. *Stem Cell Res. Ther.* **11**, 256 (2020).
56. Tracking peripheral immune cell infiltration of the brain in central inflammatory disorders using [Zr-89]oxinate-4-labeled leukocytes. ClinicalTrials.gov. https://clinicaltrials.gov/ct2/show/NCT03807973. Accessed 29 Apr 2020 (2020).
57. Friberger, I. *et al.* Optimisation of the synthesis and cell labelling conditions for [^{89}Zr]Zr-oxine and [^{89}Zr]Zr-DFO-NCS: A direct in vitro comparison in cell types with distinct therapeutic applications. *Mol. Imaging Biol.* **23**, 952–962 (2021).
58. Bansal, A. *et al.* Novel ^{89}Zr cell labeling approach for PET-based cell trafficking studies. *EJNMMI Res.* **5**, 19 (2015).
59. Bansal, A. *et al.* [^{89}Zr]Zr-DBN labeled cardiopoietic stem cells proficient for heart failure. *Nucl. Med. Biol.* **90–91**, 23–30 (2020).
60. Lee, S. H. *et al.* Feasibility of real-time in vivo ^{89}Zr-DFO-labeled CAR T-cell trafficking using PET imaging. *PLoS ONE* **15**, e0223814 (2020).
61. Patra, M. *et al.* An octadentate bifunctional chelating agent for the development of stable zirconium-89 based molecular imaging probes. *Chem. Commun. (Camb).* **50**, 11523–11525 (2014).
62. Deri, M. A. *et al.* p-SCN-Bn-HOPO: A superior bifunctional chelator for ^{89}Zr ImmunoPET. *Bioconjug. Chem.* **26**, 2579–2591 (2015).
63. Pandya, D. N. *et al.* Polyazamacrocycle ligands facilitate ^{89}Zr radiochemistry and yield ^{89}Zr complexes with remarkable stability. *Inorg. Chem.* **59**, 17473–17487 (2020).
64. Rudd, S. E., Roselt, P., Cullinane, C., Hicks, R. J. & Donnelly, P. S. A desferrioxamine B squaramide ester for the incorporation of zirconium-89 into antibodies. *Chem. Commun. (Camb).* **52**, 11889–11892 (2016).
65. Chomet, M. *et al.* Head-to-head comparison of DFO* and DFO chelators: Selection of the best candidate for clinical ^{89}Zr-immuno-PET. *Eur. J. Nucl. Med. Mol. Imaging.* **48**, 694–707 (2021).
66. Klasen, B., Lemcke, D., Mindt, T. L., Gasser, G. & Rösch, F. Development and in vitro evaluation of new bifunctional ^{89}Zr-chelators based on the 6-amino-1,4-diazepane scaffold for immuno-PET applications. *Nucl. Med. Biol.* **102–103**, 12–23 (2021).
67. Pandey, M. K. *et al.* Improved production and processing of ^{89}Zr using a solution target. *Nucl. Med. Biol.* **43**, 97–100 (2016).
68. Pandey, M. K. *et al.* A new solid target design for the production of ^{89}Zr and radiosynthesis of high molar activity [^{89}Zr]Zr-DBN. *Am. J. Nucl. Med. Mol. Imaging.* **12**, 15–24 (2022).
69. Pandey, M. K., Engelbrecht, H. P., Byrne, J. P., Packard, A. B. & DeGrado, T. R. Production of ^{89}Zr via the ^{89}Y(p, n)^{89}Zr reaction in aqueous solution: Effect of solution composition on in-target chemistry. *Nucl. Med. Biol.* **41**, 309–316 (2014).
70. Pandey, M. K. & DeGrado, T. R. Cyclotron production of PET radiometals in liquid targets: Aspects and prospects. *Curr. Radiopharm.* **14**, 325–339 (2021).
71. Abou, D. S., Ku, T. & Smith-Jones, P. M. In vivo biodistribution and accumulation of ^{89}Zr in mice. *Nucl. Med. Biol.* **38**, 675–681 (2011).
72. Larenkov, A. *et al.* Preparation of Zirconium-89 solutions for radiopharmaceutical purposes: Interrelation between formulation, radiochemical purity. *Stabil. Biodistrib. Mol.* **24**, 1534 (2019).

Acknowledgements

This study was funded by the Division of Nuclear Medicine, Mayo Clinic, Rochester, MN USA, and the International Atomic Energy Agency, Vienna, Austria.

Author contributions

A.B., performed radiolabeling, imaging studies, and contributed to manuscript writing. S.S., performed ^{89}Zr purification, imaging studies and contributed to manuscript writing. B.K., designed and synthesized Hy_3ADA^5-NCS and Hy_3ADA^5-SA chelators. F.R., designed Hy_3ADA^5-NCS and Hy_3ADA^5-SA chelators and edited the manuscript. M.K.P., designed the study, produced ^{89}Zr, guided the study and edited the manuscript.

Competing interests

AB and MKP are inventors of the [^{89}Zr[Zr-DBN based cell labeling technology [US20180043041A1].

Additional information

Supplementary Information The online version contains supplementary material available at https://doi.org/10.1038/s41598-022-19953-4.

Correspondence and requests for materials should be addressed to M.K.P.

Reprints and permissions information is available at www.nature.com/reprints.

Publisher's note Springer Nature remains neutral with regard to jurisdictional claims in published maps and institutional affiliations.